Interlayer exciton in transition metal dichalcogenide semiconductors for 2D Optoelectronics

*Yuanda Liu, Ahmed Elbanna, Weibo Gao, Jisheng Pan, Zexiang Shen and Jinghua Teng**

Dr. Yuanda Liu, Ahmed Elbanna, Dr. Jishen Pan, Prof. Jinghua Teng
Institute of Materials Research and Engineering, Agency for Science, Technology and Research (A*STAR), 2 Fusionopolis Way, Singapore 138634, Singapore
E-mail: jh-teng@imre.a-star.edu.sg

Ahmed Elbanna, Prof. Weibo Gao, Prof. Zexiang Shen
Division of Physics and Applied Physics, School of Physical and Mathematical Sciences, Nanyang Technological University, 50 Nanyang Avenue, Singapore 637371, Singapore

Prof. Weibo Gao, Prof. Zexiang Shen
The Photonics Institute and Centre for Disruptive Photonic Technologies, Nanyang Technological University, 50 Nanyang Avenue, Singapore, 639798 Singapore

Abstract

Optoelectronic materials that allow on-chip integrated light signal emitting, rerouting, modulation, and detection are crucial for the development of high-speed and throughput optical communication and computing technologies. Interlayer excitons in 2D van der Waals heterostructures, electrons and holes bound by Coulomb interaction but spatially localized in different 2D layers, have shown unique enticing properties and started to attract intense attentions for their huge potentials in novel interlayer exciton devices and fascinating underlying physics. Here, we provide a general view of these 2D-confined controllable hydrogen-like bosonic particles and present the state-of-the-arts with respect to these frontier concepts and prototyping unities. Staggered type-II band alignment enabled us to expand the interlayer direct bandgap from the intrinsic visible in monolayers up to near-IR or even mid-IR (3-8 μm) spectrum. Owing to large exciton banding energy together with ultra-long lifetime, room-temperature exciton devices and observation of quantum behaviours have been demonstrated. With these progress, we can anticipate that future studies of interlayer excitons will not only allow us to construct all-exciton information processing circuits, but that they will also continue to enrich the panoply of ideas on quantum phenomena.

1 Introduction

Increasing demand for high-speed and high-throughput telecommunication technologies calls for the shift of signal processing from electronic to optical domain. Excitonic devices can convert light into excitons, manipulate excitons by means of electric or magnetic fields, and convert excitons back to light. Of particular importance are devices on the basis of interlayer excitons, which are formed when the electrons and the holes reside in two distinct spatially separated layers. The spatial separation and formation of excitons in two different layers gives rise to unique promising properties, such as the expansion of the photoresponse wavelength to near infrared (IR) or even mid-IR, remarkably increased exciton lifetime, and creation of an oriented non-zero electric dipole moment with repulsive mutual interactions.[1–5] High-performance interlayer exciton devices have been demonstrated including light emitters, photodetectors and exciton flux modulators, which can act as the elemental device candidates for the construction of interlayer exciton information processing circuit.[6–10]

In a simplified way, excitons are usually visualized as hydrogen-atom-like a pair of electron and hole, bounded together by the electrostatic Coulomb interaction. It is the lowest electronic excited state of the materials, and therefore play a fundamental role in their optical and electrical properties. This Bosonic quasi-particle is both electrically and optically active, different from electrons and photons in which the trajectory of an electron is non-observable optically while a photon is not reactive directly to an electric field. Interlayer excitons were previously observed in conventional direct bandgap III-V quantum well structures,[5,11,12] where two GaAs quantum wells are separated by an insulating AlGaAs barrier layer. With the advent of two dimensional (2D) materials, such as metallic graphene and semiconducting transition metal dichalcogenides (TMDCs) as well as insulating hexagonal boron nitride (hBN), it has become possible to form new types of heterostructures by combining TMDCs of different chemical compositions. The advantages of interlayer excitons using 2D materials include high-quality single crystalline in 2D limit, large binding energies (> 100 meV), spin-valley polarization, van der Waals

bonding with atomic-resolution tunable interval distance, and generation of moiré pattern by arbitrary rotating angle between the two layers. The staggered type-II band alignment of 2D heterostructures induces efficient charge separation and the formation of interlayer excitons with energy ranging from visible to IR. The large exciton binding energy assures the stability of excitons at elevated temperatures, in view of the effective thermal energy of ~25 meV at 300 K. Direct-bandgap interlayer excitons have two degenerate copies of energy gaps located at the K and K′ valleys of the Brillouin zone,[13,14] suggesting unique applications that make use of the valley degrees of freedom. The atomic thickness of TMDCs bilayers, in combination with high-quality hBN dielectric layer, is particularly well suited for applications of large electric field and electrical manipulation of interlayer excitons. Furthermore, the bonding between two single crystalline sheets by van der Waals force offer an enticing playground with virtually unlimited stacking configurations for engineering and manipulating interlayer excitons.

In particular, the crystal orientation alignment of the two monolayers create a new material playground with properties utterly different from the constituent components. This degree of freedom provides an unprecedented and effective way to tune the electronic band structures of the semiconducting heterostructures. This is inaccessible for traditional semiconductors, such as III-V[2,15] and II-VI[16] compound semiconductors, in which heterostructured quantum wells are commonly epitaxially grown in high-vacuum reactors at high temperatures. Lattice mismatch would inevitably result in defects or distorted structures near the covalent interface. Achieving a variety of exciton properties in traditional semiconductors normally requires changing the chemical composition or via doping. In addition, it remains a challenge to epitaxially grow a heterostructure consisting two monocrystalline films with a controlled twist angle. The ability to modulate the exciton properties in a van der Waals material simply by stacking with selected single crystalline components with alternation of the twist angle therefore opens the door to a whole new field of research.

Since the release of the first experimental report in this field in 2014,[17] various proof-of-concept device applications have been demonstrated, covering high performance light-emitters and broadband detectors as well as exciton flux routers, to name a few. In this review, we seek to highlight the latest progress of researches on 2D interlayer excitons strongly confined within planar lattices of TMDCs by surveying the mechanisms of their unique physical properties. This may shed light on the development of all exciton information processing circuit that uses the bosonic particle-excitons as the information carrying media, in contrast with electrons and photons in integrated electronic and photonic circuit, respectively. Finally, an outlook is given to future research directions including interlayer exciton insulator, exciton superfluidity, and pressure-dependent interlayer coupling enhancement.

2 Interlayer excitons in TMDCs heterostructures

Most 2D TMDCs are semiconductors that have an energy bandgap, such as MX_2, where M = Mo, W, Hf; X = S, Se, Te. They experience a transition from indirect bandgap in non-monolayers to direct bandgap in monolayers, forming a promising library for excitonic optoelectronic devices.[13,14] Excitonic process between direct bandgaps is preferred for many optoelectronic applications. We take light emitting process as an example to interpret the reason. Semiconductors with direct energy bandgap have higher radiative recombination rate than those with indirect bandgaps, by avoiding the involvement of the absorption or emission of phonons. When free electrons and holes are responsible for the radiation recombination in a semiconductor, a continuum of possible energies for both free electrons and free holes will result in a rather broad range of photon emission energies. When excitons are formed, or in other word, the electron and the hole are bounded together, the photon emission will have a narrower emission energy. Albeit kinetic energy of excitons will lead to a broadened spectrum, it is not as broad as the free carrier spectrum. The exciton binding energy in TMDCs monolayers is in the range of 100-300 meV,[18] which enables excitons to hold together at room and even elevated temperature. In 2D monolayers, the excitons are trapped in the atomically thin planar plane, which will further narrow the energy spread. This is also the reason why moiré excitons trapped in moiré potentials have a much narrower emission (absorption)

spectrum (as discussed in detail below). Therefore, direct bandgap intra- and interlayer excitons in TMDCs are preferred for the fabrication of optoelectronic devices. In the following, we will discuss interlayer excitons after reviewing intralayer excitons in monolayers, from which the heterostructures inherit the unique properties.

2.1 Intralayer excitons in monolayers

Figure 1a summarizes the photoluminescence (PL) peak position for monolayers[19,20] and heterostructures[6,21–23] of some 2D semiconductors as comparing with GaN[24,25], GaAs[26], InP[27] and Si[28]. Figure 1b shows the typical room-temperature PL spectra of monolayer WSe_2, $MoSe_2$, WS_2, and MoS_2, respectively.[19] The samples were prepared by mechanically exfoliation from bulk single crystals. The PL peaks correspond to the A-exciton resonances, locating at the visible-near-IR wavelength from 636 nm to 792 nm (Figure 1b). The typical room-temperature absorbance spectra are shown in Figure 1c, indicating the absorption energy of A and B excitons. The A absorption resonances matche the PL peaks in both their position and width, signifying direct-bandgap luminescence. A and B excitons arise from direct bandgap transitions between the maxima of split valence bands and the minimum of the conduction band, all located at the K point of the Brillouin zone. The splitting can be traced back to the strong spin orbit coupling, which lifts the spin degeneracy of the valence and conduction band (Figure 1d-f). While the splitting is relatively small for the conduction band, the valence band separation reaches values of approximately 200 meV in molybdenum-based and 400 meV in tungsten-based TMDCs.

2.1.1 Large exciton binding energies

The reduced dielectric screening of Coulomb interactions gives result to the formation of tightly bounded excitons. Large exciton binding energies have been predicted theoretically and were estimated experimentally. Table 1 summarizes the values for some 2D monolayers. The experimental studies, by using the combined linear absorption and two-photon photoluminescence excitation spectroscopy, have achieved a large exciton binding energy of 370 meV in monolayers of WSe_2, a representative 2D direct band gap semiconductor.[29] This value is much larger than the thermal energy at room temperature (~25

meV), and is more than two orders higher than that in conventional bulk semiconductor GaAs (4.2±0.3 meV).[30] The robust excitons renders the exciton excited states and dynamic behaviors observable at elevated temperatures, which unambiguously surpasses conventional III-V semiconductors in many optoelectronic device applications. However, different values with a disparity >70 meV were achieved independently by other groups. R. Kumar et al. fitted their room temperature absorption spectra with a series of Lorentz oscillators as well as bad-edge absorption, which yielded a E_b ~440 meV for monolayer WSe_2 on quartz.[31] While a E_b ~290±20 meV was estimate when they used a simple 2D Hydrogen model. B. Urbaszek et al. carried out the 1- and 2- photon photoluminescence excitation experiments at 4 K using monolayer WSe_2 on 90 nm SiO_2, and estimated the E_b to be 600±200 meV.[32] The possible reasons for the variation both because the dielectric environments caused by the substrates and because the models used for the fitting. Hence, more systematic studies are needed to confirm the accurate value using self-supporting monolayers.

For distances exceeding few nanometres, the screening is determined by the immediate surroundings of the material. The ideal case is vacuum environment for a suspended sample. For nomolayers on a substrate and heterostructures, the screening effect plays a fundamental role in determining the both the electronic bandgap and the exciton binding energy of 2D materials. A reduction on the order of 100 mev was observed in the exciton binding energy of monolayer WS_2, from 312 meV in bare WS_2 to 214 meV in WS_2 capped by 2L graphene.[33] In WS_2/WSe_2, the intralayer exciton binding energy and the bandgap of monolayers are reduced by ~70 meV and 100 meV, respectively.[31] However, contradicting experimental results were reported. Wilson et al. found that the binding energy of intralayer excitons in one layer is insensitive to the presence of the other layer.[34] More investigations are needed to address the contradiction and identify the reason for the large disparity range between the reported values for similar samples.

2.1.2 Valley polarization

In addition to charge and spin degree of freedom, electrons in certain materials possess a valley degree of freedom. It describes which of the multiple valleys (degenerate energy extreme) in the conduction or valence bands the electrons occupy, as schematically shown in Figure 1d-f. Electrons travel through a crystal as waves, which are described by a momentum and a spin. If a crystal has two or more crystal axes that differ in their orientations, such axes can support electron waves that are also identical apart from their momentum, which is described by valley quantum number. The term 'valley' means different axes support electrons with different momenta, which appears as a valley in a plot of energy vs. momentum. The crystal structure of monolayer TMDCs lacks an inversion centre, signifying that the electrons travelling in opposite directions encounter different energetic environments.[49] The band structure has two degenerate and inequivalent valleys at the corners of the Brillouin zone. Intervalley scattering is strongly suppressed due to the large separation in momentum space. The broken inversion symmetry allows valley polarization.

Monolayer TMDCs have two momentum valleys, at the K and K′ points in the Brillouin zone, which are time-reversal copies of each other (Figure 1f). Carriers at the K and K′ points are coupled exclusively to the left and right circularly polarized light, which is called optical dipole selection rules. Excitation by left-handed circularly polarized light results in one of these valleys being populated, whereas right–handed circularly polarized light pumps the electrons in another valley. Valley polarization degree ρ can be measured through the helicity of the resulting PL spectra by $\rho = (I(\sigma^-) - I(\sigma^+)) / (I(\sigma^-) + I(\sigma^+))$. The valley polarization in pristine monolayer MoS_2 was experimentally measured by three groups to be 30%[50], 50%[51], or 100%[52], respectively. Bilayer MoS_2 has an inversion centre, therefore no valley polarization can be observed from bilayer MoS_2. These pioneering results represent a milestone for valleytronics, and suggest new research directions on TMDCs materials such as valley Hall effect. The

optical selection rules and the valley Hall effect provide the route to optically and electrically detect and control the valley degree of freedom, forming the basis for the valley based device applications.

2.2 Interlayer excitons and bandgap engineering

Monolayer TMDCs have their optical responses limited to the red-end visible spectrum to near-IR wavelength range (as shown in Figure 1). Simply stacking two monolayers by van der Waals force forms the heterostructures. Since the first observation of spatially indirect emission from heterobilayer built from WSe_2 and MoS_2 monolayers by H. Fang et al.,[17] studies have rediscovered a rich variety of new physics processes including ultrafast charge transfer, valley polarization, strong interlayer coupling between carriers, and the creation of interlayer excitons. Owning to the existence of an out-of-plane dipole moment, applying an out-of-plane electric field can tune the emission energy and amplitude of interlayer excitons. The unique properties have yielded a new family of heterostructures with superior optoelectronic applications through customized composite layers. The important milestones are illustrated in Figure 2 with a timeline. PL[17] and EL[53] are firstly demonstrated from the p-n junctions with carefully selected the p- and n- monolayers. Afterwards, optically pumped lasing emission with ultralow threshold was realized at room temperature.[6,7] The long-lived nature of interlayer excitons leads to long distance diffusion over a distance of 5-10 μm. An out-of-plane electric field can manipulate their dynamics by creating an electrically reconfigurable potentials, and demonstrated logic operation of exciton transistors.[54,55] high performance mid-IR photoresponse enabled by interlayer excitons in WS_2/HfS_2 has provide a new promising way to fabricate room temperature photodetectors that can be extended down to mid-IR or even far-IR. These pioneering proof-of-concept devices lay the foundation for exploiting the interlayer excitons in future 2D heterostructured optoelectronic applications.

2.2.1 Tunable wavelength from Near-IR to Mid-IR

The photoactive range of interlayer excitons is determined by the band-energy alignment of the constituent materials. When two monolayer TMDCs are stacked together by the van der Waals interaction,

the band alignment is determined by the work function of the constituent single layers, the interlayer interaction and the alignment of the crystal axes of the two layers. Selection of the parent materials from the 2D library enables the engineering of the optical bandgap from visible to near-IR and mid-IR. Figure 3a presents the interlayer PL spectra from $MoSe_2/WS_2$, WS_2/WSe_2, $MoSe_2/WSe_2$ and MoS_2/WSe_2 heterobilayers, respectively. These heterostructure forms type-II band alignment, and interlayer excitons in the system emit in the near-IR range (1.0-1.6 eV). The interlayer exciton emission in $MoSe_2/WS_2$, WS_2/WSe_2, $MoSe_2/WSe_2$ heterobilayers stem from the direct bandgap formed between the K valleys of the monolayer Brillouin zones. For WSe_2/MoS_2 heterostructure, both direct and indirect emission can be observed dependent on the crystal orientation angle between monolayers. The momentum-indirect interlayer exciton in WSe_2/MoS_2 results in the emission at around 770 nm, which was formed by coupling the MoS_2 conduction-band edge with local minima in the WSe_2 valence band edge.[56] The hole resides at the Γ point and the electron is located in the K valley. Liu et al. observed the direct interlayer exciton emission at around 1,200 nm (~1.0 eV), and demonstrated room temperature nanocavity lasing emission.[6] O. Karni et al. reproduced this direct interlayer transition between the K valleys.[57] Their theoretical model on the basis *ab initio* calculations suggested that the hybridization of states at the Γ point renders the K-Γ transition a mixed inter- or intralayer transition, yielding an interlayer exciton with a reduced static electric-dipole moment.

The interlayer exciton emission wavelength can be further expanded to mid-IR range by carefully screening 2D materials. Luckman and his coworkers[8] identified the unique band alignment in WS_2/HfS_2 heterostructure, where interlayer exciton interaction allows the optical absorption and emission around 48 μm (Figure 3b). The sizeable charge delocalization and interlayer exciton accumulation at the interface result in a greatly enhanced oscillator strength of the interlayer exciton and a high responsivity of the photodetector. These findings represent crucial steps towards the understanding and control of interlayer

excitons in these heterostructures with sharp interfaces, and shed light on the development of van der Waals devices.

2.2.2 Ultra-long lifetime

Due to their spatial separation, the wave functions of the electrons and holes have less overlap, suppressing the electron-hole exchange interaction.[61] The spatial distance of the two monolayers is less than 1 nm, for instance ~0.65 nm for MoS_2/WSe_2, and can be further widened by inserting a dielectric hBN layer.[62] This leads to a long population lifetime higher than nanosecond, 10^2-10^3 times longer than that of intralyer excitons (~ps). This is because the recombination rate of an exciton is proportional to the probability that the electron and the hole occupy the same location.

In $MoSe_2/WSe_2$ heterobilayer it was measured to be ~1.8 ns at 20 K.[60] The atomically thin van der Waals heterostructure is particularly well suited for application of large electric field (up to about 1 V/nm) and for electrical control of interlayer excitons. An electric field antiparallel to the interlayer exciton dipole moment can reduce the recombination rate as it pulls the two carriers apart, thereby increasing the lifetime to 600 ns.[63] Homobilayer WSe_2 has interlayer exciton with lifetime that can be tuned by electric field from ~2 ns to ~8 ns at 4 K.[55] The ultralong lifetime of interlayer excitons in hetero- or homobilayer can be further prolonged by separating these two TMDCs monolayers with insertion of a hBN layer.

The spin-valley locking leads to an extremely long valley lifetime. This is because a change of valley pseudospin requires a rare event with a large momentum transfer (from K to K′ valley) and an electron spin flip at the same time. J. Kim et al. observed that the valley-polarized resident holes in WSe_2 exhibit an intervalley scattering lifetime of more than 40 μs at 10 K.[64] The ultrafast electron transfer process in MoS_2/WSe_2 interface results in resident holes with a lifetime not limited by the decay of the electrons in MoS_2 layer. C. Jin et al. extracted the valley lifetime in WS_2/WSe_2 heterostructures to be ~20 μs. This ultralong valley polarization lifetime enables a valley current diffusion length over 20 μm.[22] Longlived

interlayer excitons are of great interest and render promising opportunities for room-temperature nanolasers, valleytronics and high-temperature exciton condensation.

2.2.3 Large exciton binding energy

The distance between electrons and holes for interlayer excitons is larger than that of the intralayer excitons in the monolayers, therefore the interlayer excitons are weakly bound comparing to intralayer excitons, leading to reduced binding energy. Even so, the binding energy of interlayer exciton in 2D heterostructures is still over 100 meV, as summarized in Table 1.[65] The binding energy of 1s interlayer excitons in WSe_2/WS_2 bilayer on diamond substrate was measured to be 126±7 meV.[47] The free space binding energy of interlayer excitons in $MoSe_2/WSe_2$e is predicted to be 246 meV[44] or 260 meV[45] using their theoretical models. Recently it was reported that the binding energy of interlayer exciton in WS_2 and monolayer HfS_2 is ~350 meV while reducing as the number of HfS_2 layers increasing.[8] The large interlayer exciton binding energy has enabled the observation of high-temperature Bose-Einstein exciton condensation in $MoSe_2/WSe_2$.[66] The phenomenon persists above 100 K, which is improved remarkably as compared with less than 10 K in conventional semiconductors (Cu_2O)[67–70]and coupled quantum wells[1,71,72] . Owing to the large exciton binding energy in MoS_2/WSe_2, room temperature high-performance near-IR lasing emission was demonstrated by Liu et al.[6]

2.2.4 Moiré excitons

For the hetero-bilayer formed using two monolayers that have same or similar lattice constants, a new lattice interference pattern emerges by offsetting the top layer with the bottom one. This in-plane lattice periodicity is described in terms of a moiré pattern, and the periodic distribution of the in-plane electronic potentials is the moiré potential. The name was borrowed from the French term moiré, which refers to a type of silk fabric that has a similar visual effect.Moirépatterns have a periodicity greater than that of the individual patterns that form it, giving rise to a new material platform with properties completely different from those of the components. The electronic bandgap of the resulted

heterostructure will be tuned by the moiré superlattice at the nanoscale. The moiré superlattices as well as the energy potentials can be modified by rotating the lattice orientation angle of the component monolayers relative to each other. The periodic variation of the atomic arrangement leads to ordered array of potential energy extremum in the real space, which will affect the propogation of electrons as well as excitons and thus is optically visible and can be monitored by using interlayer excitons. The ability to obtain controlled moiré patterns will make this physical phenomenon a rich toolbox for classic/quantum optoelectronics.

The moirésuperlattice was first demonstrated in graphene, with emerging new properties such as superconductivity and ferromagnetism. The magic angle is 1.1° for bilayer graphene.[73,74] When the bands of the moiré superlattice are half filled, interactions between the two layers create electron correlations that lead to the electrons becoming localized, creating an insulating phase resembling a Mott insulator. If the charge carrier density is electrostatically tuned away from half filling, the bilayer was turned into superconductor with a critical temperature of 1.7 K.[74] This opens a door to enter a new world.

Triggered by the exciting results observed in graphene, the exploration of moiré superlattices in other 2D materials is taking off. The electronic band structures of the TMDCs bilayers depend on the relative twist angle and the species of monolayers. The periodic sites in the moiré superlattice form the local minima or maxima in the bandgap of the heterostructure. The electrons in the twist angle TMDCs hetero-bilayer can be excited by light and at near magic angle the interlayer excitons will be trapped in individual minima forming localized moiréexcitons. The moirésupercell includes four inequivalent sites with near but nonequal trapping energies, thereby emitting recombination luminescence with four peaks in the spectrum. The supercell repeats periodically in the plane of the heterostructure.

Recently, moiré excitons in heterobilayers, which include $MoSe_2/WSe_2$ [23,75–77], WS_2/WSe_2 [78], $MoSe_2/WS_2$ [58], and $MoSe_2/MoS_2$ [79], have been studied. K. Tran et al. and K. L. Seyler et al. reported the pioneering work presenting the impact of moiré potentials on optical emission in $MoSe_2/WSe_2$ heterostructure.[23,75] When the component $MoSe_2$ monolayer and WSe_2 monolayer are aligned with a

small twist angle (~2 degree), several nearly equally spaced interlayer exciton resonances were spectrally resolved at low temperature, as shown in Figure 4a-b. The spectrum can be fitted with four Gaussian functions (Figure 4a). The resonance energies are repeatable across different locations with an alomost constant peak spacing of 22±2 meV. They attribute these resonances to excitonic ground and excited states confined within the moiré potentials. The interlayer exciton PL intensity for 20 degree twist angle has a magnitude more than two orders weaker than that for 2 degree (Figure 4b). The strong PL intensity in small angle twisted sample is due to aligned Brillouin zone corners. Narrow linewidth around 100 μeV was observed in the PL spectrum, which is comparable to those of quantum emitters reported in WSe_2 monolayer[80,81] and hBN[82] . The PL spectrum exhibit valley polarization behaviour, a Stark shift under application of an out-of-plane electric field[83], and a Zeeman splitting with an magnetic field[75,84].

In layer aligned WS_2/WSe_2 heterostructure, the generation of moiré exciton states manifest as multiple energent absorption peaks around the original WSe_2 A exciton resonance.[78] Figure 4c shows the exciton absorption spectra measured from a 0.5±0.3 degree aligned WSe_2/WS_2, compared to another sample with a large twist angle. Three prominent peaks emerge in the spectrum of near-zero twist angle at 1.683, 1.739 and 1.776 eV, whereas the large-twist-angle heterostructure shows only a WSe_2 A exciton peak at 1.715 eV. They described this phenomena using a theoretical model, in which the periodic moiré potential is much stronger than the exciton kinetic energy and generates multiple flat exciton minibands.

A growing interest has developed in twisted homobilayers, in which the moiré lattice is governed only by the relative twist angle.[85–89] In WSe_2/WSe_2 homo-bilayers, with tuning the twist angle, constant variation of the PL peak energy and intensity of moiré excitons was observed.[89] The exciton binding energy is renormalized by up to a factor of two, and their lifetime exhibits an enhancement by more than an order of magnitude. The existence of a flat band in the electronic structure was further verified using scanning tunnelling spectroscopy.[90]

The moiré pattern in the superlattice can be directly visualized.[62,78,85,91,92] [93] Figure 4d shows the atomic-resolution scanning transmission electron microscopy images from WSe_2/WS_2 heterostructures.[78] This image shows a uniform triangular lattice pattern over the whole measured region with a well-defined periodicity of about 8 nm, consistent with the formation of a moiré superlattices. Piezoresponse force microscopy (PFM), a technique provides information about the local electromechanical response, can visualize the moirésuperlattices through detecting the electric polarization and electromechanial response, which is induced by strain gradients present within moirésuperlattices.[94] Figure 4e shows the PFM amplitude and phase of twisted bilayer WSe_2, displaying the map of the moiré patterns. Anderson et al. developed a secondary electron microscope (SEM) technique to directly image the moiré domains.[85] Figure 4f shows the image of the moiré pattern in a small angle (less than 1 degree) twisted WSe_2/WSe_2 bilayer . By comparison, PFM and SEM techniques, compared with transmission electron microscopy and scanning probe microscope, are more facile and do not require special sample preparation.

3 Device applications of interlayer excitons

Whether on applications of ultra-low threshold lasing emission and broad bandwidth photo-detection, or through development of proof-of-concept valleytronic devices and exciton transistors, interlayer excitons in 2D heterostructures are creating their identities and impacts. This section delves into some of them.

3.1 Interlayer excitonic light emission

3.1.1 Lasing emission

The ultralong lifetime (~ns) of interlayer excitons can largely relax the stringent cavity requirement for the lasing. The first interlayer exciton lasing were observed from WSe_2/MoS_2 heterostructure on L3 silicon photonic crystal cavity,[6] as schematically shown in Figure 2d. WSe_2 and MoS_2 monolayers were

mechanically exfoliated from bulk single crystals, followed by stacking onto the cavity consecutively with a dry transfer method. The $MoSe_2$ and WSe_2 heterostructure is AA stacking with a broad interlayer excitonic PL peak centring at 1128.6 nm (Inset of Figure 5a). A sharp cavity mode was observed at ~1122 nm, corresponding to the designed cavity mode of the PhCC (Figure 5a). Near the threshold of ~3×10^3 W/cm^2, nonlinear increase of cavity emission intensity together with linewidth narrowing behaviour were observed (Figure 5b), indicating that stimulated emission starts taking place. A β factor of 0.17 was estimated by fitting the log-log plot of the L-L curve to the theoretical graph on the basis of classical laser rate equations (Figure 5c). A quality factor was estimated to be ~423 using a full width at half maximum (FWHM) of 2.65 nm in the cavity emission spectrum just above the lasing threshold. Owing to the large exciton binding energy, high performance lasing behavior was well sustained at room temperature. In particular, time coherence of 2D lasers was first-ever experimentally characterized. The coherence time of MoS_2/WSe_2 interlayer exciton lasers was measured by a home-made Michelson interferometer (Figure 5d). Figure 5e shows the coherence time of lasing emission as a function of the pump power. The coherence time increases and reaches a saturation limit of ~1.7 ps when the pump power crossing the threshold. A saturation limit of ~1.7 ps is agreeable with the coherence time derived from the laser linewidth (~1.9 ps). With the conceivable evidences of both amplitude and phase, the onset of lasing action was unambiguously confirmed.

$WSe_2/MoSe_2$ hetero-bilayer integrated on a silicon nitride (Si_3N_4) grating cavity (Figure 2e and Figure 5f–i) gives rise to a nanolaser operated at 918.4 nm.[7] The heterobilayer has a type-II band alignment, forming a three-level system for the injected carriers (Inset of Figure 5f). Intralayer excitons are excited by a pump laser in the WSe_2 layer (solid wavy line). Some electrons transfer to the lower $MoSe_2$ conduction band on a fast (10-100 fs) timescale (dotted line), while others recombine as intralayer excitons with lifetimes of 1-10 ps (dash-dotted wavy line). Without the cavity, the interlayer excitons (dashed line) recombine with a lifetime on the order of 1 ns (Ix) in contrast to a lifetime on the order of

100 ps (Ixc). The grating cavity provides optical feedback when photons are coupled to its resonance. The grating period, thickness and fill factor were carefully selected to obtain a high Q factor and match it to the exciton resonance at zero in-plane wavenumber, K = 0. The linewidth of the cavity mode emission is ~1.36 nm above the pump threshold (Figure 5g). Photon occupancy shows a superlinear increase. Linewidth narrowing is consistent with the onset of stimulated emission into the cavity mode. The threshold pump power is 0.18 μW, corresponding to a threshold carrier density of 5.7×10^{10} cm^{-2}, in good agreement with the density (8×10^{10} cm^{-2}) required for the transparency condition. The cavity mode fully covers the 2D heterostructure, supporting extended spatial coherence. Spatial coherence measurements were performed using a retro-reflector Michelson interferometer setup. Spatial images of coherence were recorded by a CCD (Charge-coupled devices). Below threshold, the emission is too weak for $g^{(1)}$(r,-r) measurements. Near threshold, the image is rather noisy with a clear pattern. Above threshold, a clear spatial coherent pattern emerges, showing a high $g^{(1)}$(r,-r) near r ≈ 0, as shown in Figure 5h and i.

3.1.2 Electrically driven light emission

Electrically driven luminescence is of great importance for practical applications. Ross and his coworkers[53] were the first reporting 2D interlayer exciton electroluminescence. Their device is an electrostatically defined lateral p-n junction devices on $MoSe_2/WSe_2$ hetero-bilayers. The cartoon in Figure 6a shows the p-n junction design. The right side of the gap is the hetero-bilayer, and the left side is monolayer WSe_2. The p-n junction was established by setting

the back gates to opposite voltages. With V_{BG1} = -1 V and V_{BG2} = 5 V, sweeping the source-drain bias V_{SD} from -3.5 to 3.5 V shows the rectifying behavior (Figure 6b). Electroluminescence is seen from the hetero-bilayer region, as shown in Figure 6c-d. The electroluminescence peak centres at around 1.37 eV, with a slightly higher energy than the photoluminescence peak at about 1.32 eV. Most of the electrons injected in the $MoSe_2$ conduction band and the holes in the WSe_2 valence band meet in the junction, bind

into interlayer excitons, and then recombine to emit light. The electroluminescence spectrum varies with source-drain voltage V_{SD}. As V_{SD} varies from 2.3 to 3.5 V, the peak interlayer emission shifts from 1.355 to 1.38 eV. They used the photoresponse signal to extract the interlayer exciton oscillator strength, which is 2 orders of magnitude smaller than for the intralyer excitons. This is because the overlap between the spatially separated electron and hole wave functions is reduced in this lateral hetero-junction, leading to dramatically reduced interlayer exciton oscillator strength. In addition, the ground state of interlayer exciton is momentum-indirect, due to misalignment of the band edges in momentum space. Minimizing the twist angle aligns the Brillouin zones in both layers to minimize the momentum-indirect effect and thereby might facilitate the interlayer exciton emission.

3.2 Photodetection

A photodetector is a device that can convert a light signal into an electrical signal. The interlayer exciton optical absorption enables us to design interlayer exciton photo-detectors replying on strong interlayer coupling in 2D heterostructures. Bandgap engineering by selecting the work functions of the component materials can expand the photoresponse wavelength ranging from visible to near-IR and mid-IR. Recently, high performance 2D photodetectors operated in broad range of the electromagnetic spectrum have been realized. Lukmand et al. demonstrated high-performance mid-IR (4-8 μm) photodetection enabled by interlayer excitons in WS_2/HfS_2.[8] The energy band diagram of WS_2 and HfS_2 is presented in Figure 7a. HfS_2 (d^0 semiconductor) has a deep conduction band minimum and high electron mobility, in which it is favourable for interlayer exciton electrons to reside when paired with d^2 semiconductors (WS_2). The schematic diagram of the device is illustrated in Figure 6g. Different thicknesses of HfS_2 were laid on top of monolayer WS_2 to maintain a direct bandgap for optical excitation. The enhanced spatial orbital overlap and phonon-assisted momentum conservation favour the optical transition of high oscillator strength interlayer excitons. Figure 7b shows the absorption spectra of each material and heterostructures in the visible and mid-IR range. The absorption of one layer WS_2 and 3

layer HfS_2 ($1LWS_2/3LHfS_2$) centred at 0.24 eV (corresponding to wavelength ~5.2 μm). The absorption red-shifted with increasing the number of HfS_2 layers and the absorption peak is at 0.21 eV for $1LWS_2$/bulk HfS_2, which corresponds to wavelength ~5.9 μm. The device was operated in a photoconductive mode. Figure 7c-d show the I-V curve and the extracted responsivities. Peak resonsivites of 8.2×10^2 and 9.5×10^2 A W^{-1} were observed for WS_2/3L HfS_2 under laser illuminations of λ = 4.7 and 4.3 μm, respectively, at a gate voltage of +40 V. The interlayer bandgap allows electrically tuning from the mid- to long-wave infrared spectrum, as shown in Figure 7e. The responsivity under V_g = +40 V for $1LWS_2/3LHfS_2$ is as high as 8.2×10^2 A/W (4.7 μm). The lifetime of the charge carriers in the device is calculated to be ~1 ns at source drain bias of V_{ds} = -1.5 V and excitation power of 400 nW. The detector can operate at room and elevated temperature with a higher detectivity D^*, than those commercially available infrared photodetectors (Figure 5f), making it a potentially good candidate for robust mid-IR photodetection application.

Two other groups have investigated the near-IR photoresponse using interlayer exciton near-IR absorption behaviors.[95–97] Using WS_2 and MoS_2 that have no response to infrared light individually, their few layers WS_2/MoS_2 heterostructures show photo-response at 1030 nm.[95] The thickness of WS_2 and MoS_2 is 3.1 and 4.1 nm, corresponding to 4 layers and 5 layers, respectively. The WS_2 layer has higher Femi level (~39 meV) then MoS_2 layer. Electrons tend to flow from WS_2 to MoS_2 and holes move inversely, forming interlayer excitons at the heterostructure. Au nanoparticles integrated with the heterostructure were used to enhance the 1030 nm photoresponsivity from 0.008 A/W to 0.2 A/W.

Bulk $ReS_2/ReSe_2$ heterostructure was demonstrated the ability for near-IR photodetection at 1310 nm.[96] The thickness of the ReS_2 and $ReSe_2$ were 36.5 nm and 50.4 nm, respectively. The heterojunction forms a staggered bandgap alignment with an interlayer bandgap of 0.62 eV between the valence band minimum of $ReSe_2$ and the conduction band maximum of ReS_2. Application of the gate voltage enhanced the photoresponsivity up to 3.64×10^5 A/W at λ = 980 nm and 1.58×10^5 A/W at λ = 1,310 nm. Meanwhile,

no photoresponse at 1310 nm was observed from the devices with individual ReS_2 and $ReSe_2$ alone. The extension of the photodetection range to the NIR region is attributed to the interlayer optical transition between the interlayer bandgap, but without elucidating the optical properties of interlayer excitons in their devices.

$MoTe_2/MoS_2$ heterostructures show a photoresponse at the telecommunication wavelength of 1,550 nm.[97] The work function of MoS_2 is smaller than that of $MoTe_2$, and the surface potential difference between them is measured to be about 110 meV in the dark. This report did not show the optical absorption spectrum of the interlayers, on which the spectral bandwidth of the detector replies on. And the parameters of their photodiode such as responsivity and speed are also lacked. To sum up, utilizing the interlayer excitons in 2D heterostructures provides an efficient strategy to demonstrate high performance photo-detectors, especially in the long-wavelength regime, where the intrinsic energy bandgap properties of semiconductor materials are limited.

3.3 Exciton transistor

An exciton as a whole has no net electrical charges but has a dipole moment. An interlayer exciton has a dipole moment p with an out-of-plane direction due to the separation and confinement of composed electron and hole in spatially separated layers, as shown in Figure 8a.[54] Therefore, the application of a transverse electric field leads to an exciton energy shift of $\Delta E = edF_z$, where e is electron charge, d is the electron-hole separation distance in the exciton, ed is the built-in dipole moment of interlayer excitons, and F_z is the out-of-plane electric field.[98] [99] [3] [9] With a fixed exciton dipole direction, the electric field can therefore create lower or higher energy potential along the electrode and drives the confinement and spread of interlayer excitons. Figures 8b and c show the schematic and real-space emission images of

.

exciton energy offset for exciton dynamic regimes of trap, free diffusion, and spreading when applying negative, zero, and positive gate voltages, respectively.[55] The excitons will be driven toward regions of

lower energy in the 2D potential energy surface. The exciton flux can be controlled by an electric field in the propagation midway, and operated as an exciton transistor device. The laser light was illustrated on the source electrode area, generating the exciton flux that propagate away from the excitation site. When a negative voltage was applied to the gate electrode, an exciton potential well is created in the gate electrode area, resulting in the termination of the exciton flux.

The long interlayer exciton diffusion length and the operation of exciton transistors hold great promise for optical data transmission and information processing using interlayer excitons as the media. Long lifetime allows us to manipulate the excitons within the limited time slot. The large exciton binding energy, which prevents the excitons from becoming ionized into electron-hole plasma, is needed for room temperature operation of practical applications. Previously, three dimensional excitons in the bulk semiconductors (for instance Cu_2O and organics), and two dimensional excitons in coupled quantum wells (for instance GaAs/AlGaAs) have been good candidates for exciton devices.[5,12,100,101] Interlayer excitons in van der Waals heterostructures have unique properties of small exciton Bohr radius, long lifetime and tight binding, potentially enable us to develop high performance exciton devices. Recently, exciton transistors have been demonstrated on the basis of MoS_2/WSe_2, WS_2/WSe_2, and $MoSe_2/WSe_2$ hetero-bilayers, respectively.[54,63,102] D. Unuchek et al. firstly reported exciton transistor operation in MoS_2/WSe_2 heterostructures.[54] They observed interlayer exciton diffusion over a distance of 5 μm and further demonstrated ON/OFF operation of exciton transistor at room temperature, as shown in Figure 8d. The ratio of emission intensity at ON/OFF state was extracted to be larger than 100 (Figure 8e). Such a high ON/OFF ratio results from the realization of an excitonic transistor with complete suppression of emission in the OFF state.

The lifetime of interlayer exciton in $MoSe_2/WSe_2$ increases as the transverse electric field increases and can reach up to ~600 ns.[63] Because the electric field (>0.1 V/nm) is antiparallel to the interlayer exciton dipole moment, it can reduce the recombination rate by pulling the two carriers apart. The prolonged lifetime is beneficial to the long distance transport of the interlayer excitons. it is demonstrated

that the electrically neutral interlayer excitons can propagate across the whole sample (~15 μm) under the manipulation of potentials by an electrostatic out-of-plane electric field. Charged interlayer excitons (or interlayer trions) are interlayer excitons coupled with another charged particles. A negative (positive) interlayer trion consists of an interlayer exciton and one electron (hole). As a quasiparticle that is somewhat similar to an exciton, charged interlayer excitons can be manipulated by an in-plane electric field, as compared with out-of-plane electric field of neutral interlayer excitons. Jauregui et al. also demonstrated the electrically controlled drift motion of charged interlayer excitons across the sample (~10 μm). They observed that a higher source-drain voltage give rise to a higher concentration of drifted interlayer trions.

However, these works has not discussed the role of moiré potential, which was identified to have a profound influence of exciton diffusion.[102,103] When the moiré period reduced at a larger twist angle, excitons could tunnel between supercells and diffuse over an even longer distance. However, in a moiré superlattice with a large supercell and deep potential, interlayer excitons may be completely localized. Yuan et al.[102] conducted the time-dependent measurement of exciton population profiles and showed that the interlayer excitons are more mobile in 60° twisted WS_2/WSe_2 hetero-bilayers than that in 0°. Therefore, the twist angle needs to be taken into consideration carefully, when using heterostructures as the active materials.

In comparison with mechanically stacked van der Waals heterostructures, naturally stacked bilayers have a clean interface, thus providing a very high quality of heterostructures with a higher PL emission efficiency and a longer lifetime of interlayer excitons. Naturally occurring 2H stacked bilayer of WSe_2 is an indirect bandgap semiconductor with its valence band maximum and conduction band minimum located at the K and Q points of the Brillouin zone, respectively. The lowest-energy optical transitions in bilayer WSe_2 thus happens between the K and Q valleys. Using interlayer excitons in bilayer WSe_2, Y. Liu et al. demonstrated excitonic switching on the basis of the unidirectional movement of excitons.[55] The ON/OFF ratio is around unity outside the drain electrode and increases to ~6 on the drain electrode

area, indicative of the functionality and the accuracy of the device. The star circuit with three exciton transistors was configured to demonstrate a point-to-point movement to implement device functionality of exciton circulation. The exciton flux movement longer than 10 μm was observed. The essential advantages of the excitonic transistor are the all-optical input-output signal processing, the miniaturization of device dimensions, and the flexibility of low-voltage electrical driving scheme.

4 Conclusions and Perspectives

There has been tremendous progress since the first paper[17] was published on interlayer coupling between monolayer WSe_2 and MoS_2. This work has reviewed the physical mechanisms of the unique properties of interlayer coupling, and the state-of-the-arts of devices on the basis of TMDCs van der

Waals heterostructures. As they are active both electrically and optically, they have potentials for novel high performance optoelectronic device applications. In particular, the dependence on alignment angles has offered an unprecedented approach to manipulate their electronic properties, which leads to the 'twistronics'. Taking into consideration of the excellent properties presented by these 2D interlayer excitons, next we present our pperspective and outlook to the potential research directions and remaining research challenges.

Exciton insulator

In 1960s, it was proposed that if the exciton binding energy is greater than the bandgap in a semiconductor, the material would behave as an exciton insulator.[104,105] This is a novel strongly interacting insulating phase, different from bandgap insulator and topological insulator. In an exciton insulator, it is the excitons (bosonic particles) rather than electrons (fermions) determine the physical properties. Normally an exciton is formed by an excited electron in the conduction band and a hole in the valence band. In exciton insulator, valence-band electrons would spontaneously form excitons. Exciton

insulators have been predicted to host many novel properties, including crystallized excitonium, and exciton superconductivity. Up to now, the nature of the exciton insulator remains inconclusive, and compelling experimental evidences are still absent. It is straightforward to predict that the exciton insulator transition occurs in small-bandgap semiconductors or semimetals. In 2D materials the screening of the electron-hole interaction is significantly reduced, resulting in a large exciton binding energy > 100 meV. More strikingly, the bandgap as well as the binding energy can be tuned by gate voltage and compressive force. The narrow bandgap of interlayer exciton in 2D type-II heterostructures is possible, by selecting carefully the parent materials or with the help of gate voltage and compressive force, so as to the conduction of exciton binding energy exceeding the bandgap and thereby realizing a phase transition from a bandgap insulator to an excitonic insulator.

Exciton superfluidity

Exciton superfluidity means the exciton cloud can flow without dissipation or any loss of kinetic energy. Compared to commonly known bosonic systems such as liquid He-4, excitons have smaller mass, and may lead to stable condensation at higher temperature. Exciton superfluidity may have a bright future for the non-loss energy transfer and information processing, which will be a solution of the heat dissipation and high energy consumption in integrated circuits. However, excitons have short lifetime of typically picosecond in common semiconductors, which is a major obstacle to the macroscopic condensation and the long-distance superfluidity. The advent of 2D materials has provided advantages of reduced screening and atomically sharp interface. As discussed above, interlayer excitons in van der Waals heterostructures have a long lifetime (ns), due to the spatial separation of electrons and holes. Usage of interlayer excitons in homobilayer WSe_2, has enabled the demonstration of electrically controllable interlayer exciton flux diffusion as long as 10 μm.[55] The lifetime can be further prolonged by inserting a thin layer of dielectric layer such as hBN, or the application of an out-of-plane electric field. The spatial separation also leads to weak interaction, thereby mitigating the phonon-driven Peierls

instability. We may employ type-II (staggered gap) or type III (broken gap) bandgap aligned heterostructure to realize interlayer exciton superfluidity.

Pressure tunable interlayer exciton interactions

The properties of interlayer excitons not only depends on the electronic structure of the individual materials, but also the interlayer coupling between the electron and hole. By far, the coupling of interlayer excitons have been tuned via several methods including annealing, inserting dielectric layer, applying out-of-plane electric field, inducing strain by nanopillars, and forming moiré trapping potentials.[17,83,106] The van der Waals force F_{vw} between two spheres can be described by $F_{vw} = AR_1R_1/(R_1+R_1)6r^2$, where $R_1(R_2)$ is the radius of the sphere, r is the separation distance, and A is a constant. Hydrostatic pressure applied by out-of-plane force can alter the interlayer distances of van der Waals heterostructures and is expected to tune the electronic structure together with physics properties of interlayer excitons, thereby creating moiré mini-bands, and providing another degree of freedom for the manipulation of the properties of interlayer excitons.[101] However, the limited experimental results using hydrostatic pressure to study the interlayer excitons have controversial conclusions. With increasing the pressure through a diamond anvil cell, CVD grown $WSe_2/MoSe_2$ hetero-bialyers showed a pressure-induced band changeover of interlayer excitons.[107] In contrast, Ma and his coworkers[108] observed weak pressure dependence of the interlayer exciton emission energy in $MoSe_2/WS_2$ hetero-bilayer. Therefore, systematic studies are necessary to carry out at low temperatures, to reveal the specific physics mechanism of the interlayer exciton coupling.

Acknowledgements

The work was financially supported by the Agency for Science, Technology and Research (A*STAR) under Grant No. A20E5c0084 and A2083c0058.

References

[1] T. Fukuzawa, E. Mendez, J. Hong. *Phys. Rev. Lett.* **1990**, *64*, 3066.

[2] L. Butov, A. Zrenner, G. Abstreiter, G. Bohm, G. Weimann. *Phys. Rev. Lett.* **1994**, *73*, 304.

[3] A. A. High, E. E. Novitskaya, L. V. Butov, M. Hanson, A. C. Gossard. *Science* **2008**, *321*, 229.

[4] L. Butov, C. Lai, A. Ivanov, A. Gossard, D. Chemla. *Nature* **2002**, *417*, 47.

[5] M. Combescot, R. Combescot, F. Dubin. *Rep. Prog. Phys.* **2017**, *80*, 066501.

[6] Y. Liu, H. Fang, A. Rasmita, Y. Zhou, J. Li, T. Yu, Q. Xiong, N. Zheludev, J. Liu, W. Gao. *Sci. Adv.* **2019**, *5*, eaav4506.

[7] E. Y. Paik, L. Zhang, G. W. Burg, R. Gogna, E. Tutuc, H. Deng. *Nature* **2019**, *576*, 80.

[8] S. Lukman, L. Ding, L. Xu, Y. Tao, A. C. Riis-Jensen, G. Zhang, Q. Y. S. Wu, M. Yang, S. Luo, C. Hsu, L. Yao, G. Liang, H. Lin, Y.-W. Zhang, S. K. Thygesen, Q. J. Wang, Y. Feng, J. Teng. *Nat. Nanotechnol.* **2020**, *15*, 675.

[9] G. Grosso, J. Graves, A. Hammack, A. High, L. Butov, M. Hanson, A. Gossard. *Nat. Photonics* **2009**, *3*, 577.

[10] L. Butov. *Superlattices Microstruct.* **2017**, *108*, 2.

[11] M. N. Islam, R. Hillman, D. A. Miller, D. S. Chemla, A. Gossard, J. English. *Appl. Phys. Lett.* **1987**, *50*, 1098.

[12] L. Butov. *Superlattices Microstruct.* **2017**, *108*, 2.

[13] K. F. Mak, C. Lee, J. Hone, J. Shan, T. F. Heinz. *Phys. Rev. Lett.* **2010**, *105*, 136805.

[14] A. Splendiani, L. Sun, Y. Zhang, T. Li, J. Kim, C.-Y. Chim, G. Galli, F. Wang. *Nano Lett.* **2010**, *10*, 1271.

[15] F. Fedichkin, T. Guillet, P. Valvin, B. Jouault, C. Brimont, T. Bretagnon, L. Lahourcade, N. Grandjean, P. Lefebvre, M. Vladimirova. *Phys. Rev. Appl.* **2016**, *6*, 014011.

[16] Y. Kuznetsova, F. Fedichkin, P. Andreakou, E. Calman, L. Butov, P. Lefebvre, T. Bretagnon, T. Guillet, M. Vladimirova, C. Morhain. *Opt. Lett.* **2015**, *40*, 3667.

[17] H. Fang, C. Battaglia, C. Carraro, S. Nemsak, B. Ozdol, J. S. Kang, H. A. Bechtel, S. B. Desai, F. Kronast, A. A. Unal. *Proc. Natl. Acad. Sci. U. S. A.* **2014**, *111*, 6198.

[18] S. Park, N. Mutz, T. Schultz, S. Blumstengel, A. Han, A. Aljarb, L.-J. Li, E. J. List-Kratochvil, P. Amsalem, N. Koch. *2d Mater.* **2018**, *5*, 025003.

[19] F. Ceballos, P. Zereshki, H. Zhao. *Phys. Rev. Mater.* **2017**, *1*, 044001.

[20] Y. Li, J. Zhang, D. Huang, H. Sun, F. Fan, J. Feng, Z. Wang, C.-Z. Ning. *Nat. Nanotechnol.* **2017**, *12*, 987.

[21] C. Jin, Z. Tao, T. Li, Y. Xu, Y. Tang, J. Zhu, S. Liu, K. Watanabe, T. Taniguchi, J. C. Hone. *Nat. Mater.* **2021**, 1–5.

[22] C. Jin, J. Kim, M. I. B. Utama, E. C. Regan, H. Kleemann, H. Cai, Y. Shen, M. J. Shinner, A. Sengupta, K. Watanabe. *Science* **2018**, *360*, 893.

[23] K. Tran, G. Moody, F. Wu, X. Lu, J. Choi, K. Kim, A. Rai, D. A. Sanchez, J. Quan, A. Singh. *Nature* **2019**, *567*, 71.

[24] C. Hong, D. Pavlidis, S. Brown, S. Rand. *J. Appl. Phys.* **1995**, *77*, 1705.

[25] T. Mukai, S. Nagahama, T. Kozaki, M. Sano, D. Morita, T. Yanamoto, M. Yamamoto, K. Akashi, S. Masui. *Phys. Status Solidi A* **2004**, *201*, 2712.

[26] R. Lewis, D. Beaton, X. Lu, T. Tiedje. *J. Cryst. Growth* **2009**, *311*, 1872.

[27] S. Dogan, S. T˘ uzemen. *J. Lumin*. **2008**, *128*, 232.

[28] W. Bludau, A. Onton, W. Heinke. *J. Appl. Phys.* **1974**, *45*, 1846.

[29] K. He, N. Kumar, L. Zhao, Z. Wang, K. F. Mak, H. Zhao, J. Shan. *Phys. Rev. Lett.* **2014**, *113*, 026803.

[30] S. Nam, D. Reynolds, C. Litton, R. Almassy, T. Collins, C. Wolfe. *Phys. Rev. B* **1976**, *13*, 761.

[31] R. Kumar, I. Verzhbitskiy, F. Giustiniano, T. P. Sidiropoulos, R. F. Oulton, G. Eda. *2d Mater.* **2018**, *5*, 041003.

[32] G. Wang, X. Marie, I. Gerber, T. Amand, D. Lagarde, L. Bouet, M. Vidal, A. Balocchi, B. Urbaszek. *Phys. Rev. Lett.* **2015**, *114*, 097403.

[33] A. Raja, A. Chaves, J. Yu, G. Arefe, H. M. Hill, A. F. Rigosi, T. C. Berkelbach, P. Nagler, C. Schuller, T. Korn. *Nat. Commun.* **2017**, *8*, 1.

[34] N. R. Wilson, P. V. Nguyen, K. Seyler, P. Rivera, A. J. Marsden, Z. P. Laker, G. C. Constantinescu, V. Kandyba, A. Barinov, N. D. Hine. *Sci. Adv.* **2017**, *3*, e1601832.

[35] C. Zhang, A. Johnson, C.-L. Hsu, L.-J. Li, C.-K. Shih. *Nano Lett.* **2014**, *14*, 2443.

[36] A. Klots, A. Newaz, B. Wang, D. Prasai, H. Krzyzanowska, J. Lin, D. Caudel, N. Ghimire, J. Yan, B. Ivanov. *Sci. Rep.* **2014**, *4*, 1.

[37] M. M. Ugeda, A. J. Bradley, S.-F. Shi, H. Felipe, Y. Zhang, D. Y. Qiu, W. Ruan, S.-K. Mo, Z. Hussain, Z.-X. Shen. *Nat. Mater.* **2014**, *13*, 1091.

[38] A. Chernikov, T. C. Berkelbach, H. M. Hill, A. Rigosi, Y. Li, O. B. Aslan, D. R. Reichman, M. S. Hybertsen, T. F. Heinz. *Phys. Rev. Lett.* **2014**, *113*, 076802.

[39] Z. Ye, T. Cao, K. Obrien, H. Zhu, X. Yin, Y. Wang, S. G. Louie, X. Zhang. *Nature* **2014**, *513*, 214.

[40] B. Zhu, X. Chen, X. Cui. *Sci. Rep.* **2015**, *5*, 1.

[41] J.-H. Li, D. Bing, Z.-T. Wu, G.-Q. Wu, J. Bai, R.-X. Du, Z.-Q. Qi. *Chin. Phys. B* 2020, *29*, 017802.
[42] K. W. Lau, C. Cocchi, C. Draxl. *Phys. Rev. Mater.* **2019**, *3*, 074001.

[43] M.-H. Chiu, M.-Y. Li, W. Zhang, W.-T. Hsu, W.-H. Chang, M. Terrones, H. Terrones, L.-J. Li. *ACS nano* **2014**, *8*, 9649.

[44] S. Ovesen, S. Brem, C. Linderalv, M. Kuisma, T. Korn, P. Erhart, M. Selig, E. Malic. *Commun. Phys.* **2019**, *2*, 1.

[45] H. C. Kamban, T. G. Pedersen. *Sci. Rep.* **2020**, *10*, 1.

[46] X. Zhu, J. He, R. Zhang, C. Cong, Y. Zheng, H. Zhang, S. Zhang, L. Chen. *Nanoscale* **2020**, *12*, 23732.

[47] P. Merkl, F. Mooshammer, P. Steinleitner, A. Girnghuber, K.-Q. Lin, P. Nagler, J. Holler, C. Schuller, J. M. Lupton, T. Korn, et al. *Nat. Mater.* **2019**, *18*, 691.

[48] S. Mouri, W. Zhang, D. Kozawa, Y. Miyauchi, G. Eda, K. Matsuda. *Nanoscale* **2017**, *9*, 6674.

[49] H. Yu, X. Cui, X. Xu, W. Yao. *Natl. Sci. Rev.* **2015**, *2*, 57.

[50] H. Zeng, J. Dai, W. Yao, D. Xiao, X. Cui. *Nat. Nanotechnol.* **2012**, *7*, 490.

[51] T. Cao, G. Wang, W. Han, H. Ye, C. Zhu, J. Shi, Q. Niu, P. Tan, E. Wang, B. Liu. *Nat. Commun.* **2012**, *3*, 1.

[52] K. F. Mak, K. He, J. Shan, T. F. Heinz. *Nat. Nanotechnol.* **2012**, *7*, 494.

[53] J. S. Ross, P. Rivera, J. Schaibley, E. Lee-Wong, H. Yu, T. Taniguchi, K. Watanabe, J. Yan, D. Mandrus, D. Cobden. *Nano Lett.* **2017**, *17*, 638.

[54] D. Unuchek, A. Ciarrocchi, A. Avsar, K. Watanabe, T. Taniguchi, A. Kis. *Nature* **2018**, *560*, 340.

[55] Y. Liu, K. Dini, Q. Tan, T. Liew, K. S. Novoselov, W. Gao. *Sci. Adv.* **2020**, *6*, eaba1830.

[56] J. Kunstmann, F. Mooshammer, P. Nagler, A. Chaves, F. Stein, N. Paradiso, G. Plechinger, C. Strunk, C. Schuller, G. Seifert. *Nat. Phys.* **2018**, *14*, 801.

[57] O. Karni, E. Barre, S. C. Lau, R. Gillen, E. Y. Ma, B. Kim, K. Watanabe, T. Taniguchi, J. Maultzsch, K. Barmak. *Phys. Rev. Lett.* **2019**, *123*, 247402.

[58] E. M. Alexeev, D. A. Ruiz-Tijerina, M. Danovich, M. J. Hamer, D. J. Terry, P. K. Nayak, S. Ahn, S. Pak, J. Lee, J. I. Sohn. *Nature* **2019**, *567*, 81.

[59] C. Jin, E. C. Regan, D. Wang, M. I. B. Utama, C.-S. Yang, J. Cain, Y. Qin, Y. Shen, Z. Zheng, K. Watanabe. *Nat. Phys.* **2019**, *15*, 1140.

[60] P. Rivera, J. R. Schaibley, A. M. Jones, J. S. Ross, S. Wu, G. Aivazian, P. Klement, K. Seyler, G. Clark, N. J. Ghimire. *Nat. Commun.* **2015**, *6*, 1.

[61] D. Snoke. *Science* **2002**, *298*, 1368.

[62] C. Zhang, C.-P. Chuu, X. Ren, M.-Y. Li, L.-J. Li, C. Jin, M.-Y. Chou, C.-K. Shih. *Sci. Adv.* **2017**, *3*, e1601459.

[63] L. A. Jauregui, A. Y. Joe, K. Pistunova, D. S. Wild, A. A. High, Y. Zhou, G. Scuri, K. De Greve, A. Sushko, C.-H. Yu. *Science* **2019**, *366*, 870.

[64] J. Kim, C. Jin, B. Chen, H. Cai, T. Zhao, P. Lee, S. Kahn, K. Watanabe, T. Taniguchi, S. Tongay. *Sci. Adv.* **2017**, *3*, e1700518.

[65] M. Van der Donck, F. M. Peeters. *Phys. Rev. B* **2018**, *98*, 115104.

[66] Z. Wang, D. A. Rhodes, K. Watanabe, T. Taniguchi, J. C. Hone, J. Shan, K. F. Mak. *Nature* **2019**, *574*, 76.

[67] D. Snoke, J. Wolfe, a. A. Mysyrowicz. *Phys. Rev. Lett.* **1990**, *64*, 2543.

[68] A. Mysyrowicz, E. Benson, E. Fortin. *Phys. Rev. Lett.* **1996**, *77*, 896.

[69] J. L. Lin, J. Wolfe. *Phys. Rev. Lett.* **1993**, *71*, 1222.

[70] E. Fortin, S. Fafard, A. Mysyrowicz. *Phys. Rev. Lett.* **1993**, *70*, 3951.

[71] J. Kash, M. Zachau, E. Mendez, J. Hong, T. Fukuzawa. *Phys. Rev. Lett.* **1991**, *66*, 2247.

[72] Z. Vor¨ os, D. Snoke, L. Pfeiffer, K. West. *Phys. Rev. Lett.* **2006**, *97*, 016803.

[73] Y. Cao, V. Fatemi, A. Demir, S. Fang, S. L. Tomarken, J. Y. Luo, J. D. Sanchez-Yamagishi, K. Watanabe, T. Taniguchi, E. Kaxiras. *Nature* **2018**, *556*, 80.

[74] Y. Cao, V. Fatemi, S. Fang, K. Watanabe, T. Taniguchi, E. Kaxiras, P. Jarillo-Herrero. *Nature* **2018**, *556*, 43.

[75] K. L. Seyler, P. Rivera, H. Yu, N. P. Wilson, E. L. Ray, D. G. Mandrus, J. Yan, W. Yao, X. Xu. *Nature* **2019**, *567*, 66.

[76] W. Li, X. Lu, S. Dubey, L. Devenica, A. Srivastava. *Nat. Mater.* **2020**, *19*, 624.

[77] M. Brotons-Gisbert, H. Baek, A. Molina-Sanchez, A. Campbell, E. Scerri, D. White, K. Watanabe, T. Taniguchi, C. Bonato, B. D. Gerardot. *Nat. Mater.* **2020**, *19*, 630.

[78] C. Jin, E. C. Regan, A. Yan, M. I. B. Utama, D. Wang, S. Zhao, Y. Qin, S. Yang, Z. Zheng, S. Shi. *Nature* **2019**, *567*, 76.

[79] N. Zhang, A. Surrente, M. Baranowski, D. K. Maude, P. Gant, A. Castellanos-Gomez, P. Plochocka. *Nano Lett*. **2018**, *18*, 7651.

[80] A. Srivastava, M. Sidler, A. V. Allain, D. S. Lembke, A. Kis, A. Imamoglu. *Nat. Nanotechnol.* **2015**, *10*, 491.

[81] M. Koperski, K. Nogajewski, A. Arora, V. Cherkez, P. Mallet, J.-Y. Veuillen, J. Marcus, P. Kossacki, M. Potemski. *Nat. Nanotechnol.* **2015**, *10*, 503.

[82] T. T. Tran, K. Bray, M. J. Ford, M. Toth, I. Aharonovich. *Nat. Nanotechnol.* **2016**, *11*, 37.

[83] A. Ciarrocchi, D. Unuchek, A. Avsar, K. Watanabe, T. Taniguchi, A. Kis. *Nat. Photonics* **2019**, *13*, 131.

[84] P. Nagler, M. V. Ballottin, A. A. Mitioglu, F. Mooshammer, N. Paradiso, C. Strunk, R. Huber, A. Chernikov, P. C. Christianen, C. Schuller. *Nat. Commun.* **2017**, *8*, 1.

[85] T. I. Andersen, G. Scuri, A. Sushko, K. De Greve, J. Sung, Y. Zhou, D. S. Wild, R. J. Gelly, H. Heo, D. Berube. *Nat. Mater.* **2021**, *20*, 480.

[86] L. Wang, E.-M. Shih, A. Ghiotto, L. Xian, D. A. Rhodes, C. Tan, M. Claassen, D. M. Kennes, Y. Bai, B. Kim. *Nat. Mater.* **2020**, 1–6.

[87] G. Scuri, T. I. Andersen, Y. Zhou, D. S. Wild, J. Sung, R. J. Gelly, D. Brub, H. Heo, L. Shao, A. Y. Joe. *Phys. Rev. Lett.* **2020**, *124*, 217403.

[88] P. Merkl, F. Mooshammer, S. Brem, A. Girnghuber, K.-Q. Lin, L. Weigl, M. Liebich, C.-K. Yong, R. Gillen, J. Maultzsch. *Nat. Commun.* **2020**, *11*, 1.

[89] I. Paradisanos, S. Shree, A. George, N. Leisgang, C. Robert, K. Watanabe, T. Taniguchi, R. J. Warburton, A. Turchanin, X. Marie. *Nat. Commun.* **2020**, *11*, 1.

[90] Z. Zhang, Y. Wang, K. Watanabe, T. Taniguchi, K. Ueno, E. Tutuc, B. J. LeRoy. *Nat. Phys.* **2020**, *16*, 1093.

[91] A. M. Van Der Zande, J. Kunstmann, A. Chernikov, D. A. Chenet, Y. You, X. Zhang, P. Y. Huang, T. C. Berkelbach, L. Wang, F. Zhang. *Nano Lett.* **2014**, *14*, 3869.

[92] Y. Pan, S. Folsch, Y. Nie, D. Waters, Y.-C. Lin, B. Jariwala, K. Zhang, K. Cho, J. A. Robinson, R. M. Feenstra. *Nano Lett.* **2018**, *18*, 1849.

[93] A. Weston, Y. Zou, V. Enaldiev, A. Summerfield, N. Clark, V. Zolyomi, A. Graham, C. Yelgel, S. Magorrian, M. Zhou, Z. Johanna, H. David, B. Alexei, H. B. Thomas, K. Andrey, R. W. Neil, H. B. Peter, I. F. Vladimir, J. H. Sarah, G. Roman. *Nat. Nanotechnol.* **2020**, *15*, 592.

[94] L. J. McGilly, A. Kerelsky, N. R. Finney, K. Shapovalov, E.-M. Shih, A. Ghiotto, Y. Zeng, S. L. Moore, W. Wu, Y. Bai. *Nat. Nanotechnol.* **2020**, *15*, 580.

[95] G. Wang, L. Li, W. Fan, R. Wang, S. Zhou, J.-T. Lu, L. Gan, T. Zhai. *Adv. Funct. Mater.* **2018**, *28*, 1800339.

[96] S.-H. Jo, H. W. Lee, J. Shim, K. Heo, M. Kim, Y. J. Song, J.-H. Park. *Adv. Sci.* **2018**, *5*, 1700423.

[97] K. Zhang, T. Zhang, G. Cheng, T. Li, S. Wang, W. Wei, X. Zhou, W. Yu, Y. Sun, P. Wang. *ACS nano* **2016**, *10*, 3852.

[98] D. A. Miller, D. Chemla, T. Damen, A. Gossard, W. Wiegmann, T. Wood, C. Burrus. *Phys. Rev. B* **1985**, *32*, 1043.

[99] A. High, A. Hammack, L. Butov, M. Hanson, A. Gossard. *Opt. Lett.* **2007**, *32*, 2466.

[100] A. V. Zasedatelev, A. V. Baranikov, D. Urbonas, F. Scafirimuto, U. Scherf, T. Stoferle, R. F. Mahrt, P. G. Lagoudakis. *Nat. Photonics* **2019**, *13*, 378.

[101] J. Eisenstein. *Annu. Rev. Condens. Matter Phys.* **2014**, *5*, 159.

[102] L. Yuan, B. Zheng, J. Kunstmann, T. Brumme, A. B. Kuc, C. Ma, S. Deng, D. Blach, A. Pan, L. Huang. *Nat. Mater.* **2020**, *19*, 617.

[103] J. Choi, W.-T. Hsu, L.-S. Lu, L. Sun, H.-Y. Cheng, M.-H. Lee, J. Quan, K. Tran, C.-Y. Wang, M. Staab. *Sci. Adv.* **2020**, *6*, eaba8866.

[104] N. F. Mott. *Philos. Mag.* **1961**, *6*, 287.

[105] D. Jerome, T. Rice, W. Kohn. *Phys. Rev.* **1967**, *158*, 462.

[106] M. Kremser, M. Brotons-Gisbert, J. Knorzer, J. G uckelhorn, M. Meyer, M. Barbone, A. V. Stier, B. D. Gerardot, K. Muller, J. J. Finley. *NPJ 2D Mater. Appl.* **2020**, *4*, 1.

[107] J. Xia, J. Yan, Z. Wang, Y. He, Y. Gong, W. Chen, T. C. Sum, Z. Liu, P. M. Ajayan, Z. Shen. *Nat. Phys.* **2021**, *17*, 92.

[108] X. Ma, S. Fu, J. Ding, M. Liu, A. Bian, F. Hong, J.-T. Sun, X. Zhang, X. Yu, D. He. *arXiv preprint arXiv:2103.08369* 2021.

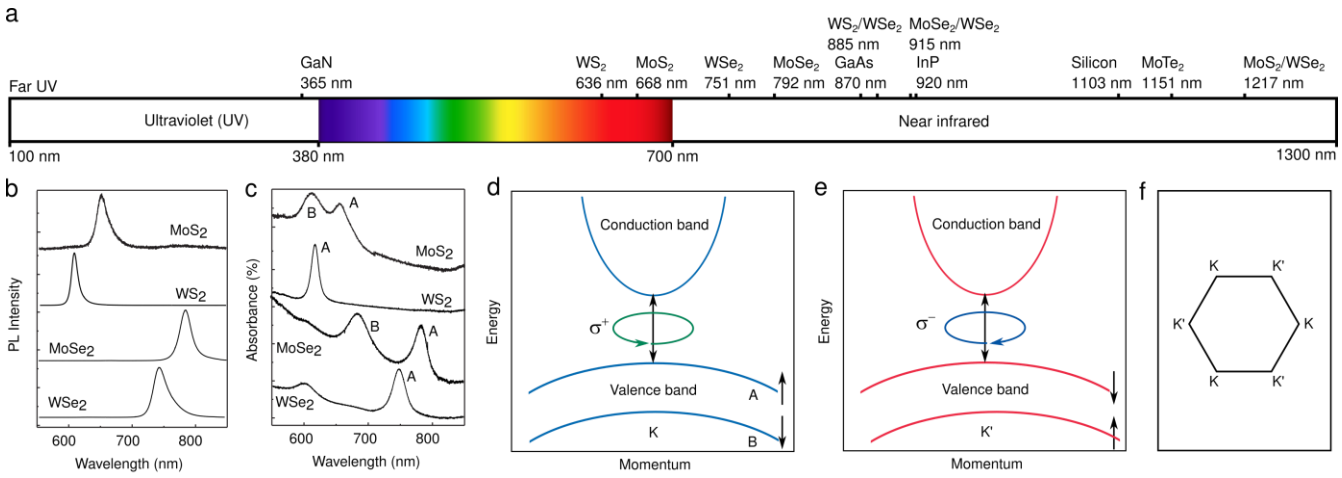

Figure 1. a) Photoluminescence peak positions of 2D monolayers and hetero-bilayers, as compared with bulk semiconductors GaAs[26], GaN[24,25], InP[27] and Si[28]. The sample temperatures are 6.4 K for GaN, 10 K for WS_2/WSe_2 [21,22], 15 K for $MoSe_2/WSe_2$ [23], 300 K for 2D monolayers and MoS_2/WSe_2 [6], respectively. Si has an indirect bandgap of 1.1242 eV corresponding to 1103 nm.[28] b)-c) Photoluminescence and absorbance spectra of monolayer WSe_2, $MoSe_2$, WS_2, and MoS_2, respectively. The curves are displayed along the vertical axis for clarity. The samples were prepared by mechanically exfoliation from bulk single crystals. Reproduced with permission.[19] Copyright 2017, American Physical Society. d)-f) Schematic of valley-dependent selection rules at K and K′ points in crystal momentum space.

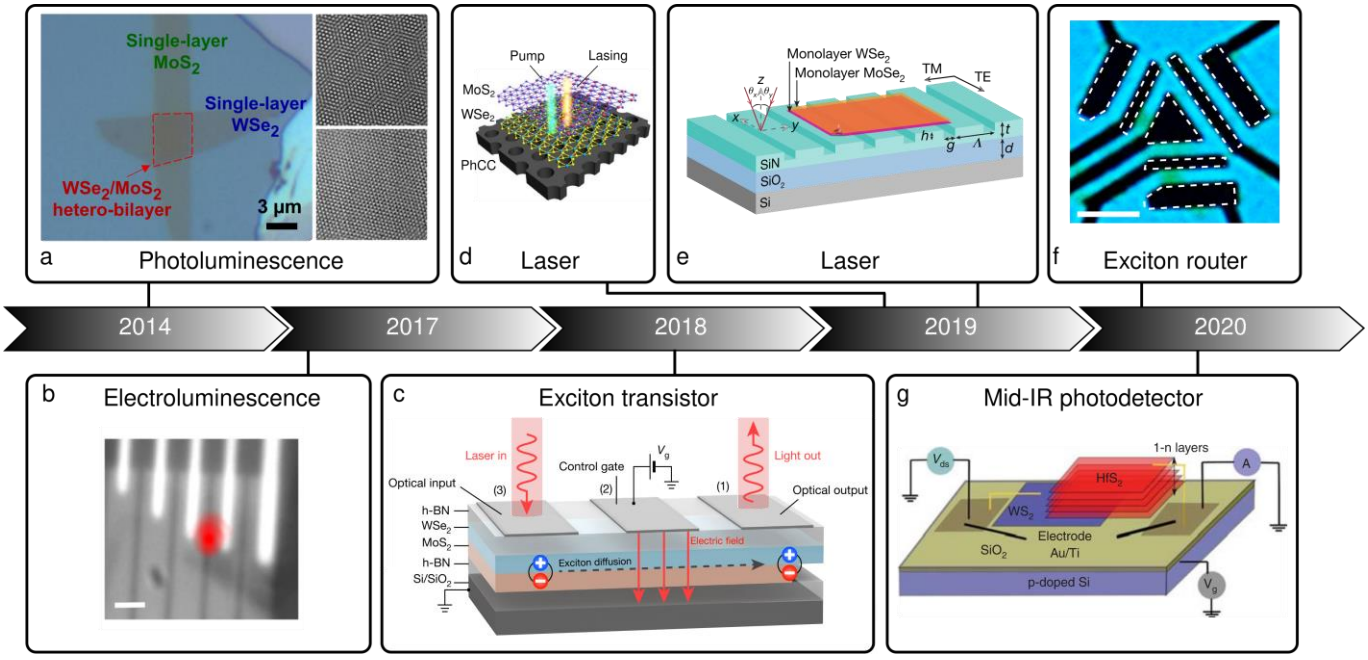

Figure 2. Timeline illustrating the history of interlayer exciton devices. a) First observation of spatially indirect emission, suggesting strong interlayer coupling of charge carriers in MoS_2 and WSe_2 monolayers. Reproduced with permission.[17] Copyright 2014, National Academy of Sciences. b) Electroluminescence from interlayer excitons in $MoSe_2/WSe_2$. Reproduced with permission.[53] Copyright 2017, American Chemical Society. c) Interlayer exciton transistor made of MoS_2/WSe_2. Reproduced with permission.[54] Copyright 2018, Springer Nature Limited. d) Room temperature lasing emission demonstrated from MoS_2/WSe_2 integrated with silicon photonic crystal cavity. Reproduced with permission.[6] Copyright 2019, American Association for the Advancement of Science. e) Lasing emission with $MoSe_2/WSe_2$ as the gain material. Reproduced with permission.[7] Copyright 2019, Springer Nature Limited. f) Exciton router operation. Reproduced with permission.[55] Copyright 2020, American Association for the Advancement of Science. g) Mid-IR photodetection with interlayer exciton absorption band in WS_2/HfS_2. Reproduced with permission.[8] Copyright 2020, Springer Nature Limited.

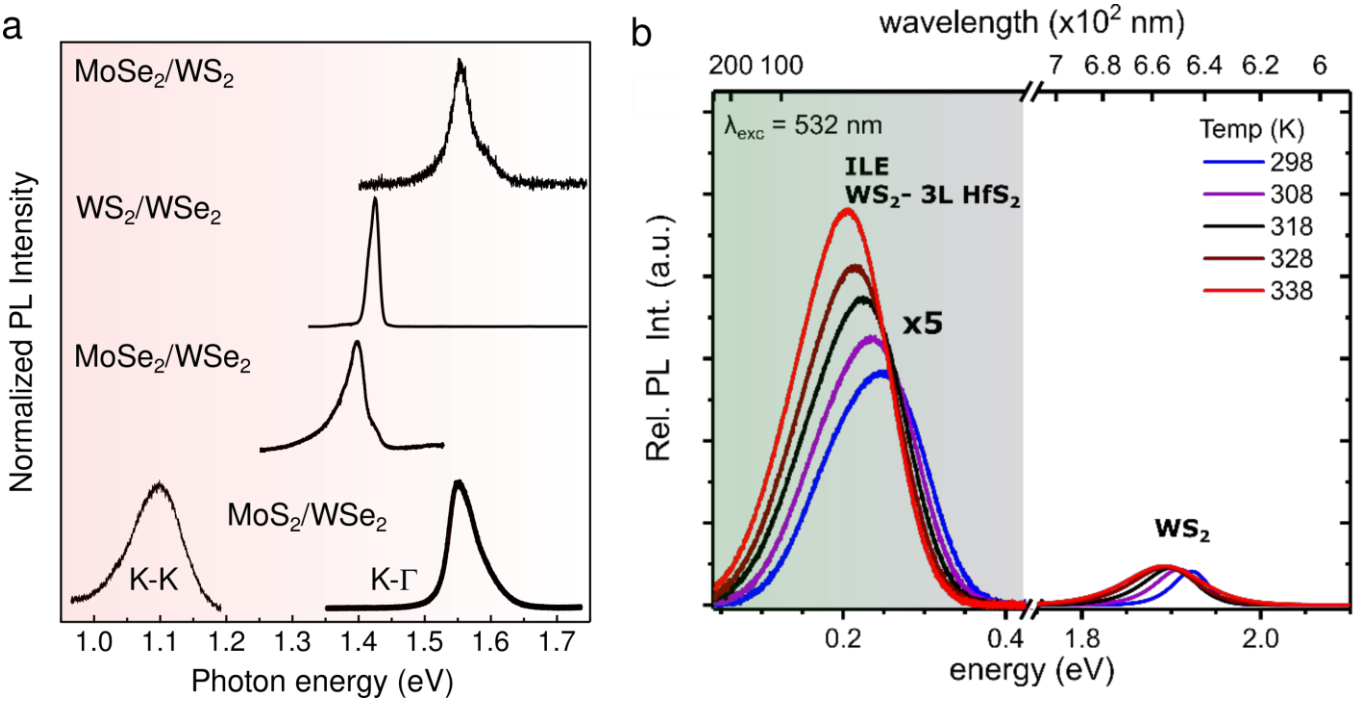

Figure 3. a) Interlayer exciton photoluminescence spectrum in $MoSe_2/WS_2$, WS_2/WSe_2, $MoSe_2/WSe_2$ and MoS_2/WSe_2 heterobilayers, respectively. The curves are displayed along the vertical axis for clarity. Reproduced with permission. $MoSe_2/WS_2$ curve[58]: Copyright 2019, Springer Nature Limited. WS_2/WSe_2 curve[59]: Copyright 2019, Springer Nature Limited. $MoSe_2/WSe_2$ curve[60]: Copyright 2015, Springer Nature Limited. MoS_2/WSe_2 high energy curve[17]: Copyright 2014, National Academy of Sciences. MoS_2/WSe_2 low energy curve[6]: Copyright 2020, American Association for the Advancement of Science. b) Mid-IR interlayer exciton emission in WS_2/3L HfS_2. Reproduced with permission.[8] Copyright 2020, Springer Nature Limited.

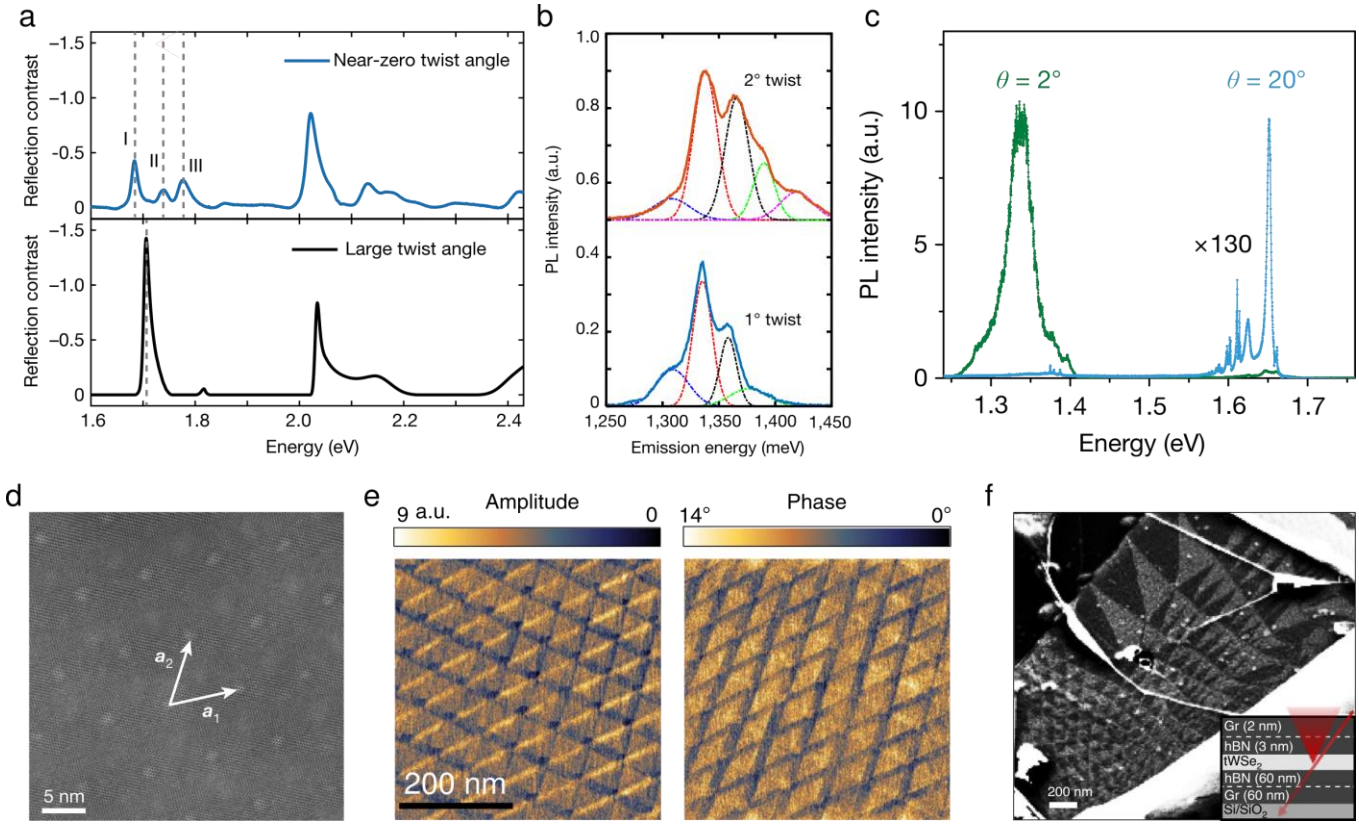

Figure 4. Moiré excitons trapped in TMDCs heterostructures. a) Photoluminescence spectra for $MoSe_2/WSe_2$ heterobilayers with twist angles of 1 and 2 degrees. Each spectrum is fitted with four (1 degree) or five (2 degree) Gaussian functions. Reproduced with permission.[23] Copyright 2019, Springer Nature Limited. b) Photoluminescence spectra for $MoSe_2/WSe_2$ heterobilayers with twist angles of 2 and 20 degrees. The intensity for 20 degree is scaled by 130×. Reproduced with permission.[75] Copyright 2019, Springer Nature Limited. c) Reflection contrast spectrum of 0.5±0.3 degree aligned WSe_2/WS_2, compared to another sample with a large twist angle. Reproduced with permission.[78] Copyright 2019, Springer Nature Limited. d) Atomic-resolution scanning transmission electron microscopy high-angle annular dark-field image of a near-zero twist angle WSe_2/WS_2 heterostructure. Reproduced with permission.[78] Copyright 2019, Springer Nature Limited. e) Piezoresponse force microscopy (PFM) amplitude and phase of twisted bilayer WS_2, showing the capability of PFM for imaging of moiré superlattices. Reproduced with permission.[94] Copyright 2020, Springer Nature Limited. f) Secondary electron microscope image of twisted bilayer WS_2, showing a reconstructed moiré pattern with trangular

AB and BA sacking domains. Inset: device schematic. Reproduced with permission.[85] Copyright 2021, Springer Nature Limited.

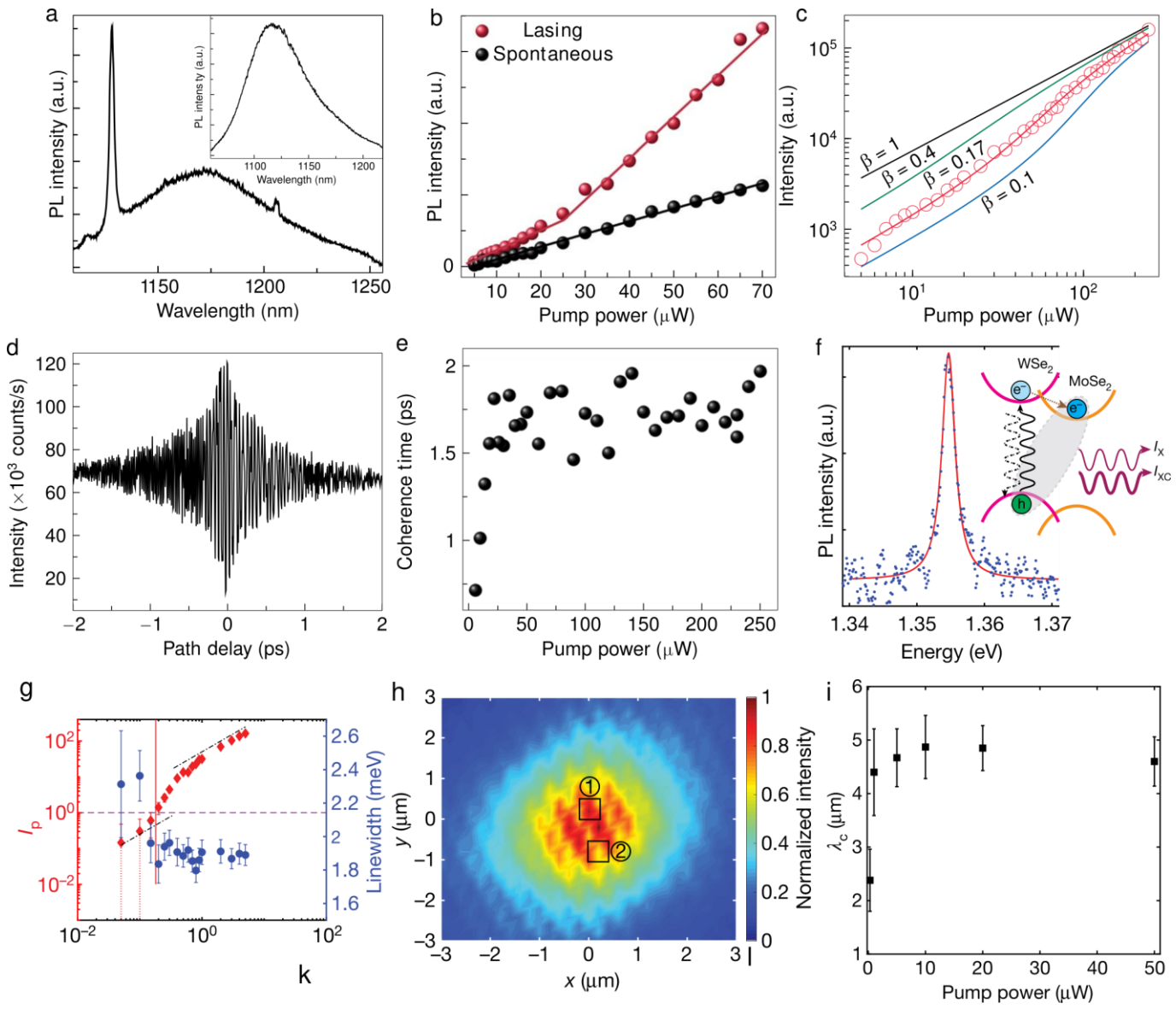

Figure 5. a) Room temperature cavity lasing mode emission spectrum. The linewidth is ~ 2.26 nm. Inset shows the room temperature off cavity spectrum of the heterobilayer for comparison. b) L-L curve showing the output intensity as a function of the excitation pump power. T = 5 K. The cavity mode emission (red dots) exhibits a 'kink', indicating the onset of superlinear emission and lasing operation, while the heterobilayer PL background emission (black dots) shows a linear dependence on the pump intensity. Solid lines are the linear fit to the experimental data. c) Log-log plot of the cavity mode emission intensity as a function of the pump power. Solid lines are the simulated results of a rate equation calculation with different β factors. Red line shows the best fit to the experimental data (red circles)

corresponding to β = 0.17. The fits of 0.1, 0.4, and 1 are also shown for comparison. d) Coherent time measurement. Raw data of emission intensity as a function of path delay at pump power of 250 μW. e) Coherence time as a function of pump power. Reproduced with permission.[6] Copyright 2019, American Association for the Advancement of Science. f) PL spectrum. The red line is a Lorentzian fit, with a fitted linewidth of 2.4 meV. Inset: band alignment and carrier dynamics of the $WSe_2/MoSe_2$ bilayer. g) The photon occupancy (red) and linewidth (blue) of the TE emission versus input pump power. The dot-dashed line indicates linear dependence, the vertical line marks P_{th}, and the horizontal purple line indicates I_p = 1. h) Interference pattern above P_{th} (20 μW). i) The coherence length λ_c versus the pump power. The error bars correspond to the 95% confidence interval of the Gaussian fit. Reproduced with permission.[7] Copyright 2019, Springer Nature Limited.

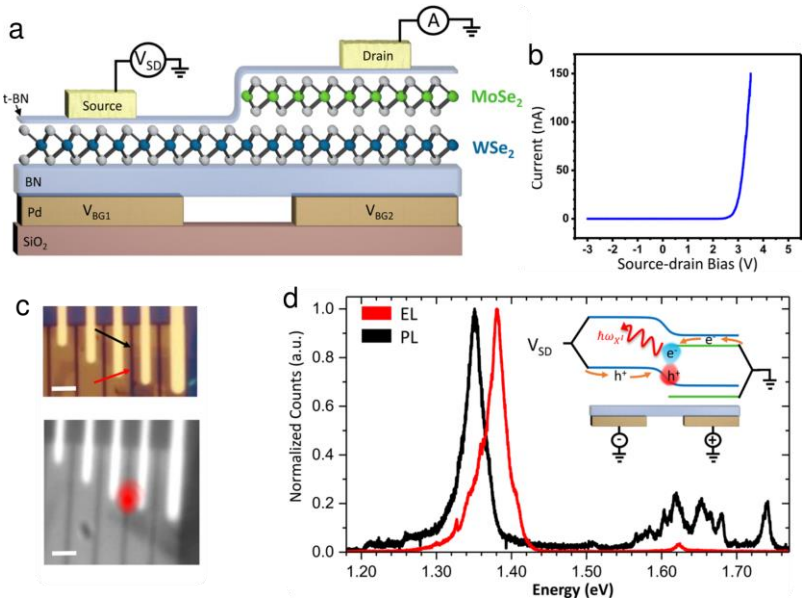

Figure 6. Electroluminescent devices. a) Carton of the $MoSe_2/WSe_2$ device structure. b). I-V curve showing diode behavior. c) Top panel shows the microscope image of device. Bottom panel shows the electroluminescence image. Scale bar: 2μm. d) Electroluminescence (red) and photoluminescence (black) spectra. Each layer is individually gated (inset). Reproduced with permission.[53] Copyright 2016, American Chemical Society.

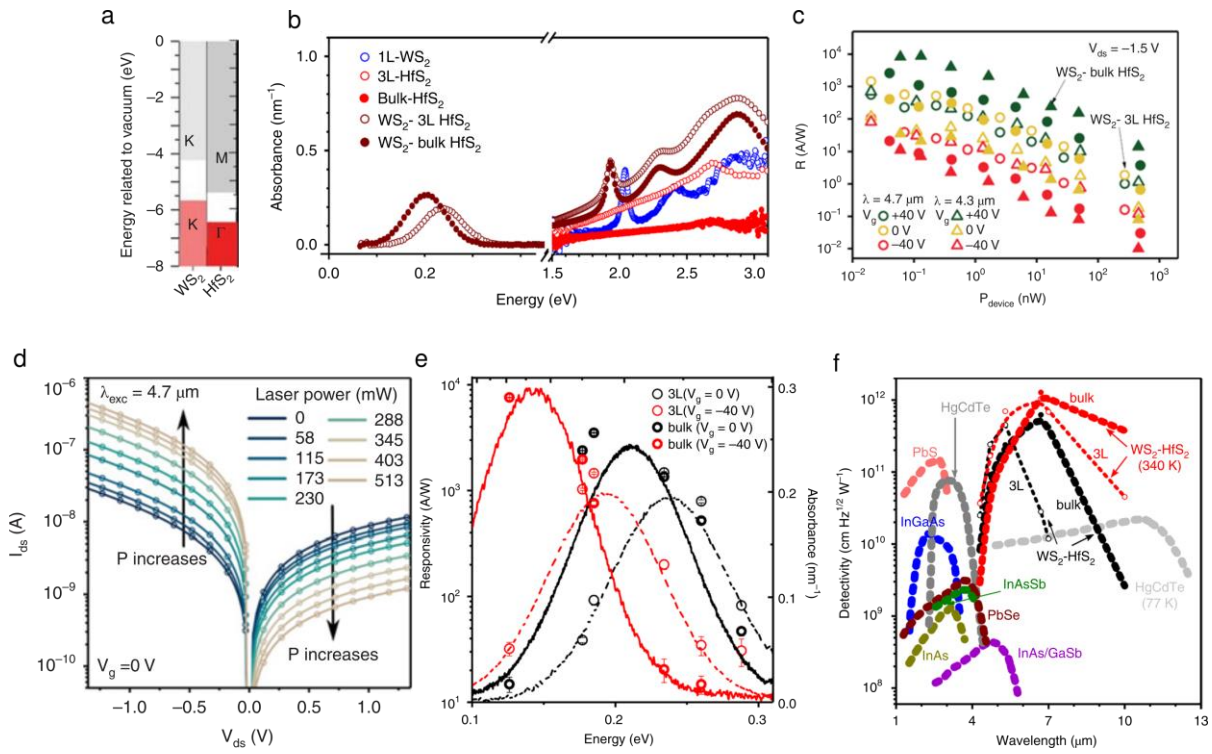

Figure 7. Room-temperature mid-IR photodetector on the basis of WS_2/HfS_2. a) Energy band diagram illustrating the gap offset between WS_2 and HfS_2. b) Absorption spectra in the visible and mid-IR ranges. 1L, one layer; 3L, three layers; bulk, ~30 layers. c) The responsivity of WS_2/3L HfS_2 and WS_2/bulk HfS_2 under two different excitation wavelengths (λ = 4.3 μm and 4.7 μm) and different gating voltages, with V_{sd} = -1.5 V. d) $I - V$ curve of the WS_2/3L HfS_2 heterostructure under different laser excitation powers (P). λ = 4.7 μm, V_g = 0 V. e) Responsivity at V_g = 0 and -40 V. V_{ds} = -1.5 V; P_{device} = 0.5 nW. f) Superior detectivity as compared with the commercially available photo-detectors at room temperature, unless otherwise specified. Reproduced with permission.[8] Copyright 2020, Nature Publishing Group.

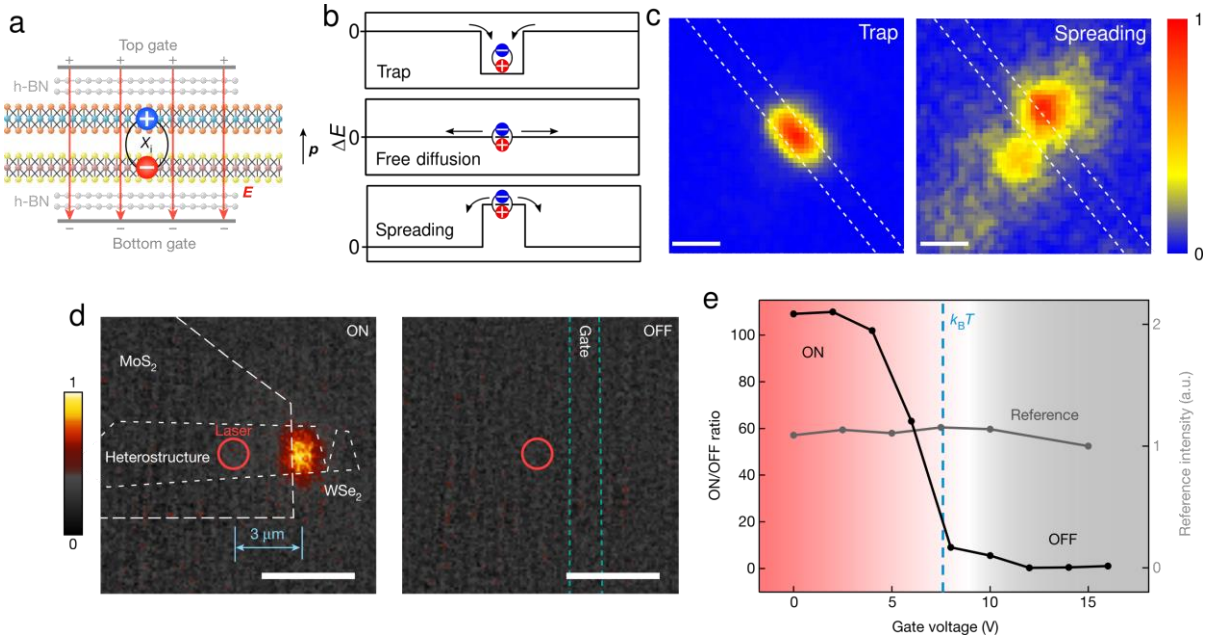

Figure 8. Mechanism and operation of interlayer exciton transistors. a) Schematic depiction of the heterostructure encapsulated in hexagonal boron nitride (hBN) and the top and bottom gates. Reproduced with permission.[54] Copyright 2018, Nature Publishing Group. b) Schematic of interlayer exciton energy offsets for exciton dynamic regimes of trap, free diffusion, and spreading when applying negative, zero, and positive gate voltages, respectively. c) Real-space emission intensity map for exciton trap, and spreading. Scale bar, 2 μm. Reproduced with permission.[55] Copyright 2019, American Association for the Advancement of Science. d) Real-space exciton emission, showing the ON and OFF state. Colour scale indicates the normalized photoluminescence intensity. Scale bar, 5 μm. e) Emission intensity profiles for ON/OFF state of the exciton transistor, showing an ON/OFF ration >100. Reproduced with permission.[54] Copyright 2018, Nature Publishing Group.

Table 1. Exciton binding energies for intralayer excitons in 2D TMDC monolayers and interlayer excitons in heterostructures. 1L, monolayer. HS, heterostructures. E_b, Exciton binding energy (meV).

1L	MoS_2	$MoSe_2$	WS_2	WSe_2	$MoTe_2$	HfS_2
E_b	240[18], 220±10[35], 570[36]	550[37]	320±40[38], 550[31], 700[39,40]	370[29], 440[31], 600±200[32],	185[41]	780[42]
HS	WSe_2/MoS_2	$MoSe_2/WSe_2$	WS_2/MoS_2	WSe_2/WS_2	$MoSe_2/MoS_2$	WS_2/HfS_2
E_b	260[43]	200[34], 246[44], 260[45]	431.39±127.818[46]	126±7[47]	90[48]	350-200[8]